Chemical Engineering Science 295 (2024) 120171

Contents lists available at ScienceDirect

Chemical Engineering Science

journal homepage: www.elsevier.com/locate/ces

A particle packing electrode model for microstructure optimization of lithium-ion batteries

Yiting Lin [a], Yunqi Cai [a], Cheng Lian [a,b,c,*], Honglai Liu [a,b,c]

[a] School of Chemical Engineering, East China University of Science and Technology, Shanghai 200237, PR China
[b] School of Chemistry and Molecular Engineering, East China University of Science and Technology, Shanghai 200237, PR China
[c] State Key Laboratory of Chemical Engineering, East China University of Science and Technology, Shanghai 200237, PR China

ARTICLE INFO

Keywords:
Performance modeling
Porous electrodes
Particle packing electrode model
Microstructure optimization
Lithium-ion batteries

ABSTRACT

The microstructure of porous electrodes has a significant impact on the performance of lithium-ion batteries (LIBs). The critical challenge in theoretical research of porous electrodes is to construct an electrode model that properly describes its microstructure while ensuring solving efficiency. In this work, a particle packing electrode (PPE) model is used to analyze the charging dynamics of LIBs, which is constructed based on the randomness distribution of the active materials. After accurately predicting the experimental data, the PPE model illustrates two key factors governing the C-rate performance: The C-rate performance depends on the Li^+ transfer in active material at low C-rate and depends on Li^+ transfer in the electrolyte at high C-rate. By optimizing the uniformity of the particle size and the orderliness of the pore structure, LIBs achieve improved performance. This model offers novel possibilities for designing and optimizing electrode microstructures of LIBs.

1. Introduction

Lithium-ion batteries (LIBs) are one of the most advanced power sources available today, boasting remarkable energy density and extraordinary cycle life (Cheng et al., 2023). The porous electrode provides a large interphase contact area, which improves the capacity of the active material at a high charge rate (C-rate) (Yi et al., 2023). At a C-rate of several hundred, individual active particles can retain 80 % of their theoretical capacity (Zhang et al., 2023). However, the C-rate performance decreased significantly as the individual particles formed a porous electrode. Designing the microstructure of porous electrodes is one of the major challenges in improving electrochemical performance (Duan et al., 2023). This microstructure depends on the ratio and spatial distribution of the electrode's active materials and the conductive binders.

Currently, tremendous efforts are being directed towards the optimization of microstructure through the utilization of innovative active materials (R. F. Service, 2019; Winter et al., 2018; Wang et al., 2022), morphological control (Zhang et al., 2023; Zhang et al., 2023), and process optimization (Le et al., 2017). However, repeated experimental performance tests are time-consuming and costly. One cost-efficient approach is using the electrochemical model to predict the performance of LIBs before manufacturing (Duan et al., 2023). The pseudo-two-dimensions (P2D) model (R. F. Service, 2019; Winter et al., 2018; Wang et al., 2022; Nguyen et al., 2020), which was pioneered by Doyle and Newman (Fang et al., 2020), is the most widely used electrochemical model for LIBs. However, its assumption of a uniform distribution of active materials fails to account for the microstructure of the electrode, resulting in deviations from actual predictions, particularly at high C-rates (Yi et al., 2023; Xia et al., 2022). To enhance the accuracy of model predictions, efforts are directed toward developing electrode models that better characterize the microstructure of porous structures, thereby rendering the prediction more realistic and effective (Weichert et al., 2022; Chang et al., 2023; Lombardo et al., 2021; Pinilla et al., 2023). Techniques such as scanning electron microscopy and X-ray tomography have facilitated the development of reconstructive electrode models (Li et al., 2022; Newman and Tiedemann, 1975; Safari and Delacourt, 2011). These models are more complex and closer to the actual electrode structures, making their predictions more accurate (Safari and Delacourt, 2011). Nevertheless, the computational complexity and cost increase, and the computation is more difficult to converge. In other words, simple models sacrifice model accuracy to obtain macroscopic performance and achieve fast simulations, while complex models sacrifice computational speed to obtain microscopic

* Corresponding author at: School of Chemical Engineering, East China University of Science and Technology, Shanghai 200237, PR China.
E-mail address: liancheng@ecust.edu.cn (C. Lian).

https://doi.org/10.1016/j.ces.2024.120171
Received 6 March 2024; Received in revised form 18 April 2024; Accepted 19 April 2024
Available online 21 April 2024

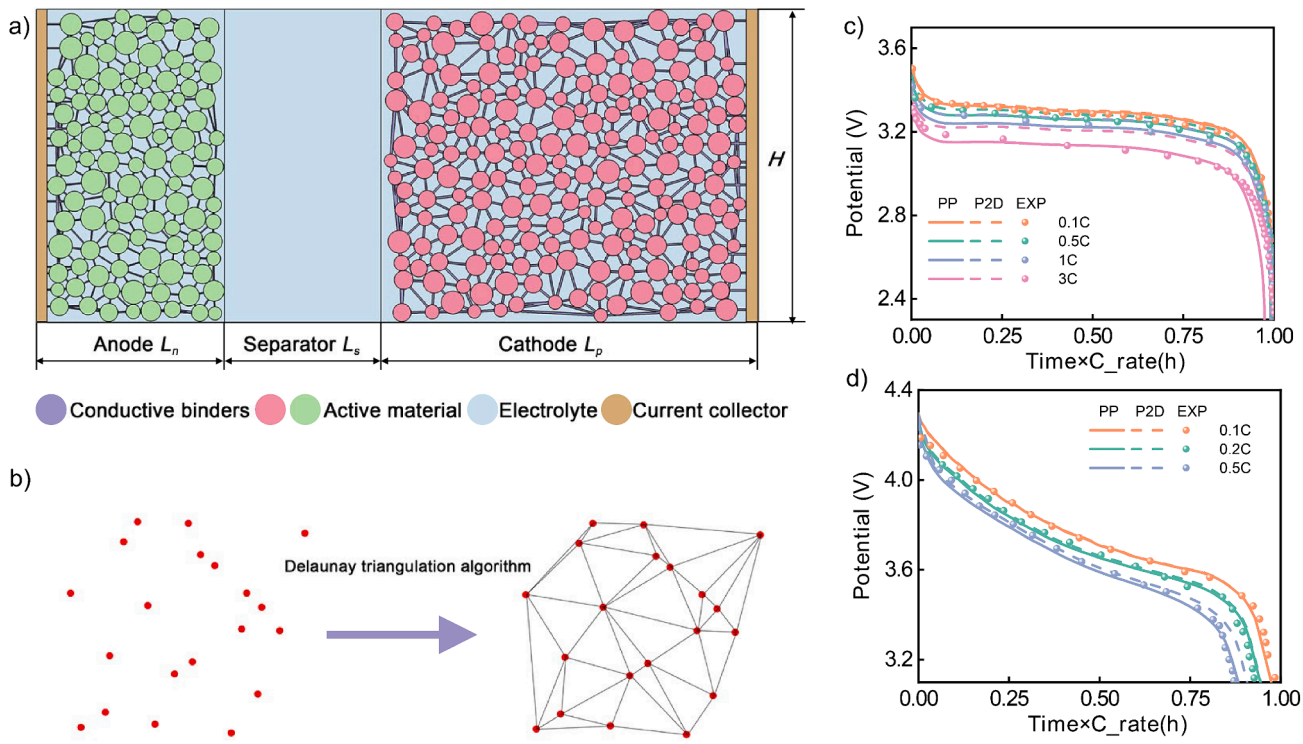

Fig. 1. a) Sketch of particle packing electrode model. b) Overview of the Delaunay triangulation algorithm. c-d) The discharging curves of c) LFE||Gr batteries with discharge current and d) NCM||Gr batteries with different C-rates. The solid lines and dashed lines correspond to the simulated results of the PPE model and the P2D model. The symbols correspond to experimental data.

performance and high accuracy.

At the level of the electrode, several parameters such as electrode formulation (Chen et al., 2022; An et al., 2021), tortuosity (Li et al., 2019; Franco, 2013; Taiwo et al., 2016), porosity (Lueth et al., 2015; Kang et al., 2022), and particle size distribution (Xu et al., 2023; Mistry et al., 2018; Trembacki et al., 2018; Hamed et al., 2020) (PSD) all contribute to the Li diffusion (Danner et al., 2016; Le Houx and Kramer, 2020; Apachitei et al.). Our previous works have used the microscopic stack-electrode (SE) model to simulate the porous electrode, demonstrating that the porous structure and pore size distribution of the electrode significantly affect its performance (Grießl et al., 2022; Narita et al., 2020; Bae et al., 2014). In this work, a near-real two-dimensional particle packing electrode (PPE) model was used to analyze the charging dynamics and performance of LIB, which consists of active material

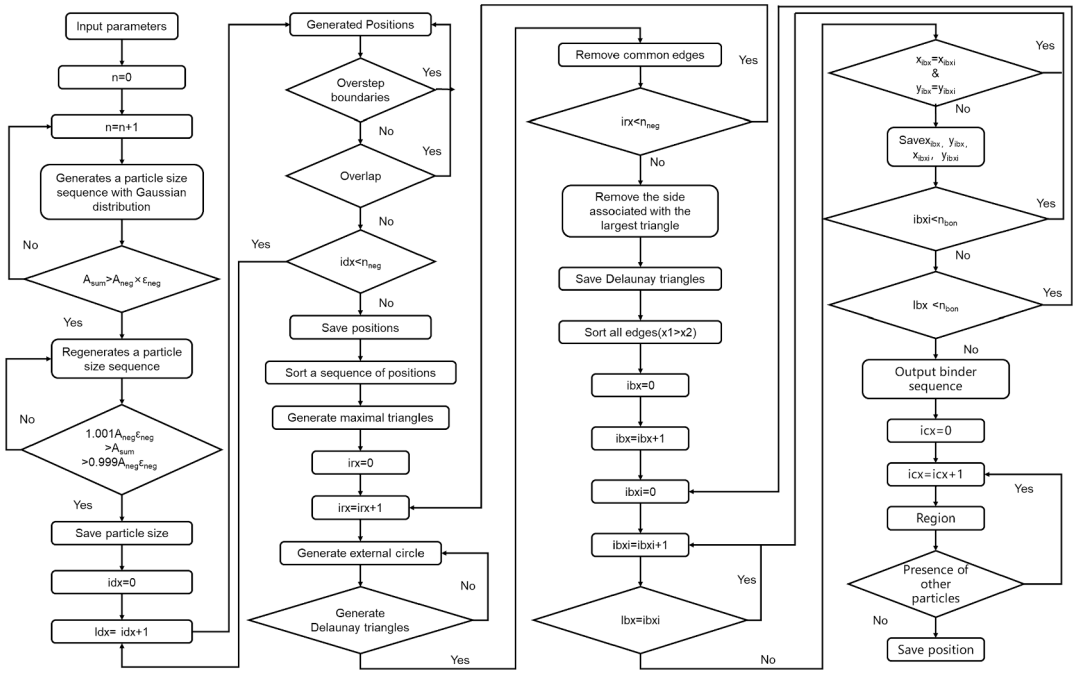

Fig. 2. The flowchart depicting the construction of the particle packing electrode model.

particles, conductive binders, and electrolyte. Notably, there is no effective tortuosity in the model equations, which avoids the errors in effective ion transport within pores introduced by the Bruggeman relation. Meanwhile, the spatial distribution of the active materials and the conductive binders allows this model to accurately analyze the microscopic charging dynamics of the electrodes and the effects of PSD, porosity, and electrode formulation on the performance of LIBs. The PPE model simulates the electrochemical process within LIB by the partial differential equations (PDEs) with given initial and boundary conditions (Abdollahifar et al., 2023). In conjunction with COMSOL Multiphysics, we analyzed the influences of different structural parameters on the electrochemical performance and provided different optimization approaches for different types of LIBs.

2. Methodology

2.1. Geometry of particle packing electrode model

Fig. 1a shows the PPE model which consists of conductive binders, active materials, electrolytes, and current collectors. In this work, the PPE model assumes that the active material particles are spherical entities and the PSD follows a Gaussian distribution. Different distributions can be realized by modifying the code. The spatial location of the active material particles within the PPE model is random and the conductive binders form rigid bridging conductive adhesive regions. The interstices among the active particles are imbued with electrolytes, effectively filling the pores.

The PPE model demonstrates a non-uniform porous electrode model by randomizing active material particles' size and position. The specified mean, standard deviation, and particle size range of Gaussian distribution ensure the randomness of particle size and avoid generating particles that are too large or too small. Furthermore, the volume of the active material generated by the particle size sequence is controlled to have an error within 0.1 % of the input information (this tolerance can be adjusted according to actual requirements). The randomization of particle positions is achieved by randomly generating particle coordinates, ensuring that the particles do not overlap and exceed the electrode area.

The conductive binders connect adjacent particles in a bridging manner, strongly correlated with the location of the active particles. In this work, the Delaunay triangulation network is applied to generate the conductive binders network (Fig. 1b), which ensures the porous electrode is stable without cross-linking conductive binders. The width of the conductive binders is determined by the total length of the Delaunay triangulation network and the partial size distribution. The boundaries of the electrodes are set as the current collectors. Notably, in extended research of PPE model, optimizing the conductive network and electrode formulation to achieve optimal power and energy densities can be accomplished by decreasing the content of conductive additives and increasing the content of active materials. The specific procedure of model construction is shown in Fig. 2.

In this work, the PPE model based on spherical active material particles is designed to analyze the specific effects of particle size and distribution of active materials on the Li^+ transfer within the electrode pores and active materials at different C-rates. Although the geometric dimensions of active material particles are variable, by adjusting the geometric structure generation modules within the model construction code, the PPE model can construct structures with different geometric features. Notably, as the battery is subjected to prolonged use, the structure and electrochemical properties of the particles undergo changes. Consequently, in advanced research, the PPE model can consider the comprehensive effects of factors such as the formation of the solid-electrolyte interphase (SEI), internal stress, and heat generation on battery performance. Moreover, while the PPE model primarily focuses on the micro-scale kinetic behavior of lithium-ion batteries, the effective integration of this model into the analysis of macro-scale thermal management and battery system behavior remains an area that warrants further exploration. In summary, the PPE model offers a novel perspective for elucidating how the microstructure of porous electrodes affects battery performance. Building on this foundation, we can make necessary refinements and optimizations to the model construction methods to meet the research demands of various application scenarios.

2.2. Governing equations of the electrochemical model

Nomenclature	
a_s	Specific surface area (m^{-1})
A	Area (m^2)
c_i	the concentration of species i in liquid phase (mol/m^{-3}(−|-))
c_l	Li^+ concentration in liquid phase (mol/m^{-3}(−|-))
c_s	Li^+ concentration in active material (mol/m^{-3}(−|-))
$c_{s,max}$	Maximum concentration of Li^+ in the active material (mol/m^{-3}(−|-))
$c_{s,e}$	Surface concentration of Li^+ (mol/m^{-3}(−|-))
D_i	Diffusion coefficient of species i in liquid phase (m^2/s)
D_s	Li^+ diffusion coefficient in active material (m^2/s)
F	Faraday constant (96485C mol^{-1})
H	Width
i_0	Exchange current density (A/m^{-2}(−|-))
L	Thickness
j_i	Current density in liquid phase (A/m^{-2}(−|-))
j_s	Current density in solid phase (A/m^{-2}(−|-))
j_r	Reaction current density (A/m^{-2}(−|-))
k_0	Reaction temperature constant ($m^{2.5}$ $mol^{-0.5}$ s^{-1})
R	Universal gas constant (Jmol^{-1} K^{-1})
r	Radius of active material particle (μm)
ϕ_s	Potential of active material (V)
z_i	Charge valency of species i
Greek letters	
a_s, a_c	Transfer coefficient
ε_s	Volume fraction of active material
ε_b	Volume fraction of conductive binder
U	Open circuit voltage
η	Over potential (V)
σ	Standard deviation of particle size
σ_s	Conductivity
Subscripts and superscripts	
0	Initial state
l	Liquid phase
s	Solid phase
SOC	State of charge

2.2.1. Electron transport

The conduction of electrons in the conductive binders' network and the active material particles. The relationship between the potential and the current density can be described by Ohm's Law:

$$\sigma_s \nabla \phi_s = j_s \tag{1}$$

Where j_s is the current density, σ_s is the conductivity, and $\nabla\phi_s$ is the gradient of the potential.

2.2.2. Ion transport

The migration and diffusion of lithium ions (Li^+) within the electrolyte which can be described by Poisson-Nernst-Planck (PNP) equation (Shodiev et al., 2022; Fu et al., 2023; Lin et al., 2022):

$$\begin{aligned} \frac{\partial c_i}{\partial t} &= -\nabla \cdot j_i \\ \nabla \cdot (\varepsilon_0 \varepsilon_r \nabla \phi) &= -F \sum_{i=1}^{n} z_i c_i \\ j_i &= -D_i \nabla c_i - \frac{D_i z_i F c_i}{RT} \nabla \phi \end{aligned} \tag{2}$$

Here, c_i, D_i, and z_i are the concentration, the diffusion coefficient, and the charge valency of species i, respectively. In addition, F, R, and T represent the Faraday constant, gas constant, and absolute temperature ($T =$

Table 1
Parameters of LFP||Gr battery model (Safari and Delacourt, 2011).

Parameter	Anode	Separator	Cathode
Thickness L/m	34×10^{-6}	30×10^{-6}	70×10^{-6}
Width H/m	60×10^{-6}	60×10^{-6}	60×10^{-6}
Area A/ m^2	1.69×10^{-7}	1.69×10^{-7}	1.69×10^{-7}
Volume fraction of active material ε_s	0.55		0.43
Volume fraction of conductive binder ε_b	0.12	0.54	0.098
Average particle radius r/m	3.65×10^{-6}		3.5×10^{-6}
Standard deviation of particle size σ	0.2		0.2
Initial SOC	0.825		0.03
Initial concentration c_0 mol·m^{-3}		1200	
Maximum solid phase concentration $c_{s,max}$ /mol·m^{-3}	31,370		22,806
Intercalation reaction constant k_0/ mol·m^2·s^{-1}	8.0×10^{-11}		3.0×10^{-11}
Solid phase conductivity σ_s/ S·m^{-1}	100		0.5
Solid phase diffusion coefficient D_s/m^2·s^{-1}	1.45×10^{-13}		3.2×10^{-13}

Table 2
Parameters of NCM||Gr battery model (Huang et al., 2022).

Parameter	Anode	Separator	Cathode
Thickness L/m	70×10^{-6}	30×10^{-6}	70×10^{-6}
Width H/m	12×10^{-5}	12×10^{-5}	12×10^{-5}
Area A/ m^2	0.95×10^{-4}	0.95×10^{-4}	0.95×10^{-4}
Volume fraction of active material ε_s	0.46		0.49
Volume fraction of conductive binder ε_b	0.063	0.8	0.127
Average particle radius r/m	12.03×10^{-6}		5.5×10^{-6}
Standard deviation of particle size σ	0.2		0.2
Initial SOC	0.90		0.03
Initial concentration c_0 /mol·m^{-3}		1000	
Maximum solid phase concentration $c_{s,max}$ /mol·m^{-3}	31,370		50060
Intercalation reaction constant k_0/ mol·m^2·s^{-1}	8.0×10^{-11}		5.0×10^{-12}
Solid phase conductivity σ_s/ S·m^{-1}	100		0.5
Solid phase diffusion coefficient D_s/m^2·s^{-1}	1.45×10^{-13}		1.18×10^{-18}

293.15 K), respectively, where ε_0 is the permittivity of vacuum and ε_r is the relative permittivity of electrolyte.

2.2.3. Electrochemical reaction

The electrochemical reaction at the interface between active material particles and electrolyte can be described by the Butler-Volmer Equation:

$$\begin{aligned} j_r &= a_s i_0 \left[\exp\left(\frac{\alpha_a F\eta}{RT}\right) - \exp\left(\frac{\alpha_c F\eta}{RT}\right) \right] \\ i_0 &= k c_e^{\alpha a} \left(c_{s,\max} - c_{s,e}\right)^{\alpha_a} c_{s,e}^{\alpha_c} \\ \eta &= \varphi_s - \varphi_e - U_{eq} \end{aligned} \tag{3}$$

Where, a_s is the specific surface area of active materials, i_0 is the exchange current density, k is the electrochemical reaction coefficient, α_a and α_c are the electrode transfer coefficient, $c_{s,max}$ is the maximum of Li^+ concentration in the active material, $c_{s,e}$ is the concentration of Li^+ on the surface of the active material particles, η is the overpotential, and U is the open circuit voltage of the battery.

2.2.4. Mass transfer

The diffusion process of Li^+ within the active material particles of anode or cathode can be described by the Fick's second Law:

$$\frac{\partial c_s}{\partial t} = \nabla(D_s \nabla c_s) \tag{4}$$

In this work, active substance particles are considered spherical particles, and their solid phase concentration can be expressed as:

$$\frac{\partial c_s}{\partial t} = \frac{D_s}{r^2} \frac{\partial}{\partial r}\left(r^2 \frac{\partial c_s}{\partial r}\right) \tag{6}$$

where c_s is the Li^+ concentration in the active material, D_s is the solid phase diffusion coefficient, ∂t and ∂r represent the variation of lithium ion concentration within the active material with time and position, respectively.

The boundary conditions are:

$$\left.\frac{\partial c_s}{\partial r}\right|_{r=0} = 0, \left.\frac{\partial c_s}{\partial r}\right|_{r=R_p} = -\frac{j_r}{a_s F} \tag{7}$$

Notably, the state of charge (SOC) of electrodes in this work are defined with:

$$\mathrm{SOC_e} = \frac{c_s - c_{s,0}}{c_{s,\max} - c_{s,0}} \tag{8}$$

Where $C_{s,0}$ is the initial concentration of electrodes.

2.3. Comparison of the PPE model and the traditional P2D model

Different with PPE model, the pseudo-two-dimensions (P2D) model assume that the active material particles are spherical and the electrodes only consist of active material, current collectors and electrolytes. Within P2D model, the Li^+ migrates along the x-direction in electrolytes and migrates along the radial (r) direction in active materials. Notably, both the active material particles and the electrolyte phase are uniformly dispersed throughout the electrode.

The P2D model, as the most widely-used, disregards the intricate microstructure of porous electrodes and uses homogenization indicators to represent the overall geometric model. The Bruggeman method is often employed to estimate the effective diffusion coefficient in the P2D model, which values the tortuosity factor as 1.5. However, there is a strong correlation between the tortuosity factor and the microstructure of porous electrodes.

In this work, $LiFePO_4$ (LFE) batteries and $LiNi_{1/3}Mn_{1/3}Co_{1/3}O_2$ (NCM) batteries are used to compare the PPE models and the P2D models. The specific model parameters are shown in Table 1 and 2:

The OCV curves of Gr (Tao et al., 2020), LFE (Lu et al., 2021) and NCM (Chung et al., 2014) electrodes were also obtained from the literatures.

Fig. 1 compares the discharging curves of LFE||Gr batteries (Fig. 1c) and NCM||Gr batteries (Fig. 1d) with different C-rates. The solid lines correspond to the simulated results of the PPE model, the dashed lines correspond to the simulated results of the P2D model, and the symbols correspond to the experiment data. The results of the PPE model are consistent with the experiment data, while the results of the P2D model have a partial deviation from the experiment data at high C-rates. The difference is that LFE batteries have a large deviation in potential during the discharging process while NCMs have a deviation in capacity. The reasons for this phenomenon are detailed in the next section. At lower C-rates (0.1C and 0.5C for LFE batteries, 0.1C and 0.2C for NCM batteries), the slower reaction rate and the uniform distribution of the Li^+ within the pores enable the uniform charging/discharging of the active material within the electrode. However, the deviation between these three data gradually increases with increasing C-rates. It is attributed that the microstructure of porous electrodes is the primary factor contributing to the significant degradation of the C-rate performance. The P2D model considers a homogenous structure and thereby significantly underestimates the impact of electrode structure on performance. The PPE model is constructed based on the randomness of the active materials particle distribution during the manufacturing of the electrode, which effectively reproduces the microstructure of the electrode. Moreover, as a two-dimensional model, the PPE model significantly enhances

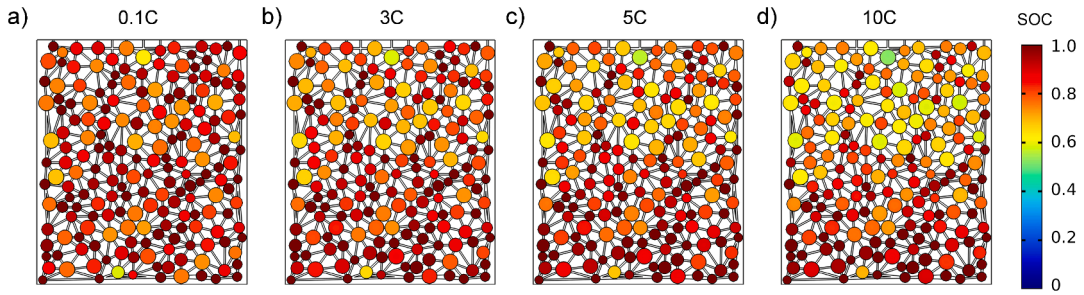

Fig. 3. The distribution of c_s of LFE electrode with $\sigma = 0.3$ at different C-rates and the end of discharging. a) 0.1C, b)3C, c) 5C, d)10C.

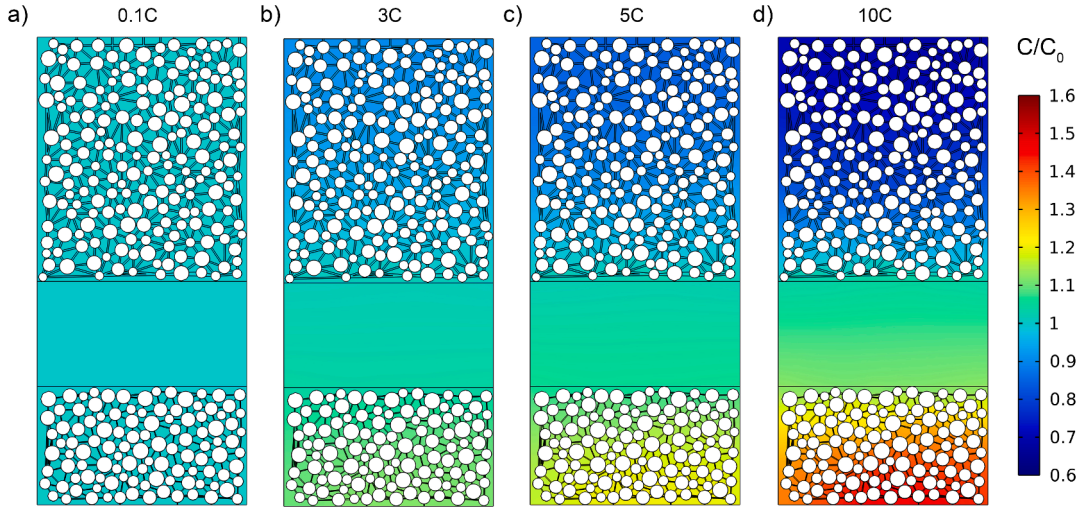

Fig. 4. The distribution of c_l of LFE||Gr batteries with $\sigma = 0.3$ at different C-rates and the end of discharging. a) 0.1C, b)3C, c) 5C, d) 10C.

computational efficiency compared to the three-dimensional reconstructive electrode models.

3. Result and discussion

As a two-dimensional and non-homogeneous, the PPE model can be solved by the finite element method to visualize the distribution of Li^+/Li concentration inside the LIB with various operating conditions. Such visualization can help us understand the micro-dynamics of LIB during the charging/discharging processes. During the discharging progress, Li^+ de-intercalates from the anode to the electrolyte and moves to the cathode. In the meantime, the electrons pass through the conductive

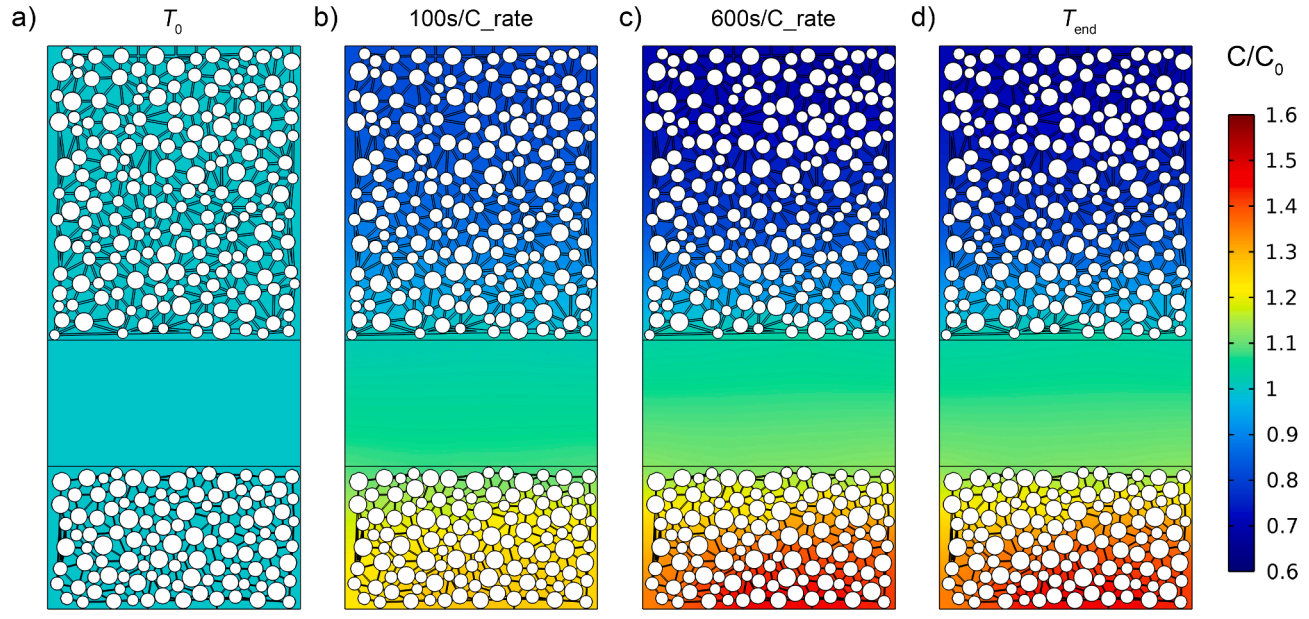

Fig. 5. The distribution of c_l of LFE||Gr batteries in the charging process with $\sigma = 0.3$ at 10C. a)T_0, b)100 s/C-rate, c) 600 s/C-rate, d)T_{ed}.

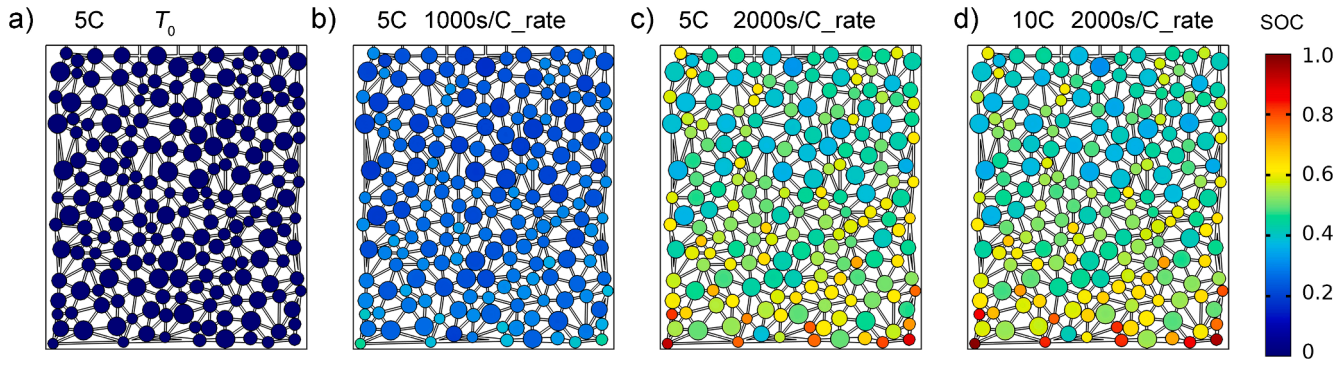

Fig. 6. The distribution of c_s of LFE electrodes in the discharging process with $\sigma = 0.3$. a) 5C and T_0, b) 5C and 1000 s/C-rate, c) 5C and 2000 s/C-rate, d) 10C and 2000 s/C-rate.

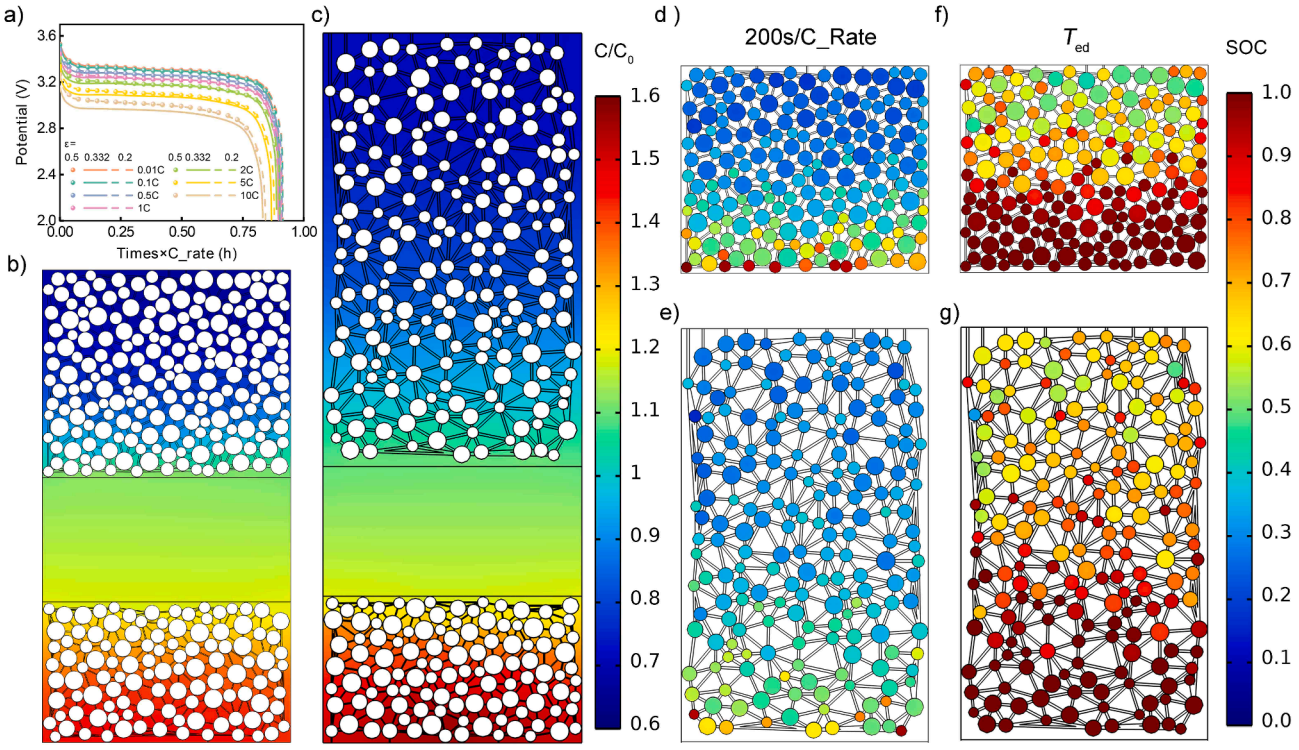

Fig. 7. a) the discharging curves of LFE||Gr batteries with different C. b-c) The distribution of c_l of LFE||Gr batteries with $\sigma = 0.3$ at 10C and the end of discharging. d-g) The distribution of c_s of LFE electrode in the discharging process with $\sigma = 0.3$ at 10C. b), d) and f) $\varepsilon = 0.2$. c), e) and g) $\varepsilon = 0.5$. d) and e) 2000 s/C-rate. f) and g) T_{ed}.

binders to the current collector and move from the anode to the cathode via the external circuit. Therefore, c_l within the anode will be higher than that within the cathode, forming a concentration gradient distribution. Fig. 3 shows the distribution of c_s of LFE electrode and Fig. 4 shows the distribution of c_l of LFE||Gr batteries at different C-rates and the end of discharging. At 0.1C, the Li^+ oxidized from the interface of the anode can quickly migrate to the cathode interface, where they are reduced and intercalated to the cathode. At the same time, the slow reaction rate resulted in a uniform distribution of c_s (Fig. 3a). Hence, the c_l and c_s are almost independent of spatial position (Fig. 4a). Notably, the distribution of c_l is almost independent of time, and the distribution of c_s is determined by the interfacial reaction rate without being limited by diffusion. As the C-rates increase, the electrodes exhibit elevated rates of Li^+ generation/consumption compared with the Li^+ diffusion rate, leading to a corresponding enhancement of the concentration gradient of the c_l and c_s in the z-direction. The magnitude of this gradient depends on the C-rates and the complexity of the porous structure. For the distribution of c_l, the concentration gradient stabilizes after the concentration gradient is established. Specifically, at a C-rate of 10C, this stabilization is attained within a period of 600 s/C-rate, accounting for roughly 20 % of the overall charging process.

The corresponding distributions of c_l of LFE||Gr batteries in the charging process are shown in Fig. 5. Notably, c_s is unevenly distributed throughout space, especially at 3C and 5C (Fig. 3). In this case, the Li^+ concentration gradient in the liquid phase does not significantly affect the surface reaction of the active material particles, and the concentration inside the active particles is almost independent of the z-direction. The Li^+ concentration gradient increases with increasing current, but the Li^+ reduction reaction consumes essentially the same amount of Li^+ that migrates form the surface of Gr in the electrolyte. However, due to the particle size of the cathode material particles, smaller size particles have lower capacity and shorter charging times, while larger size particles require longer reaction times. Therefore, c_s of the LFE particles is dependent on the PSD (Fig. 6). As the SOC of the active particles

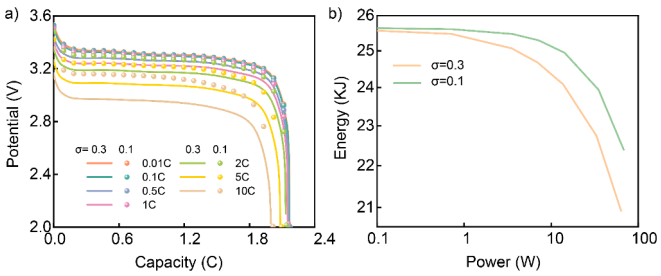

Fig. 8. a) The discharging curves of LFE||Gr batteries at different σ and C-rates. b) The Ragone curves of LFE||Gr batteries with $\sigma = 0.3$ and 0.1.

approaches 0 or 1, the local potential increases or decreases dramatically, thereby increasing the polarization voltage of the LIBs.

One of the important parameters for the microstructure of electrodes is porosity (ε), which is often adjusted using the calendering process in experiments. The calendering process does not alter the volume of active material and conductive binders. Therefore, in this work, we fixed the PSD of the electrode's active material and calculated the thickness of the electrode at the same porosity based on different porosities, then randomly regenerated the position sequence of the active material particles. The specific construction steps are shown in the Supporting Information. Fig. 7a compares the discharging curves of electrode films with different ε. As the value of ε decreases, the polarization voltage of the discharge curve exhibits a decreasing trend and then increases. Fig. 4d, Fig. 7b and c show the distribution of Li^+ concentrations in the electrolyte phase and within the active material particles at 10C. The low porosity of the electrode results in a higher thickness, which further leads to a longer ion transport distance. However, the loose arrangement of active substances results in a lower tortuosity of the electrode (Fig. 3d and Fig. 7e-g). The higher porosity increases the electrode curvature while reducing the ion transport distance on the thickness of the batteries. Therefore, the calendering process essentially optimizes the effect of electrode thickness and tortuosity on the actual transmission distance of Li^+.

To investigate the effect of PSD on the LIBs' performance, the PPE models with cathode's particle size dispersion (σ) of 0.3 and 0.1, respectively, were generated in this work. The specific construction steps are also shown in the Supporting Information. Fig. 8 shows the corresponding discharging curves and the Ragone curves. With the increase of C-rates, the polarization voltage increases. A more uniform PSD within the active material particles reduces the polarization and improves the C-rate performance of the batteries. At $\sigma = 0.3$, discharge curves are almost identical below 1C, the polarization of the discharge curves increases with increasing current. At $\sigma = 0.1$, the particle size of the active material is nearly uniform. The discharge curves show no

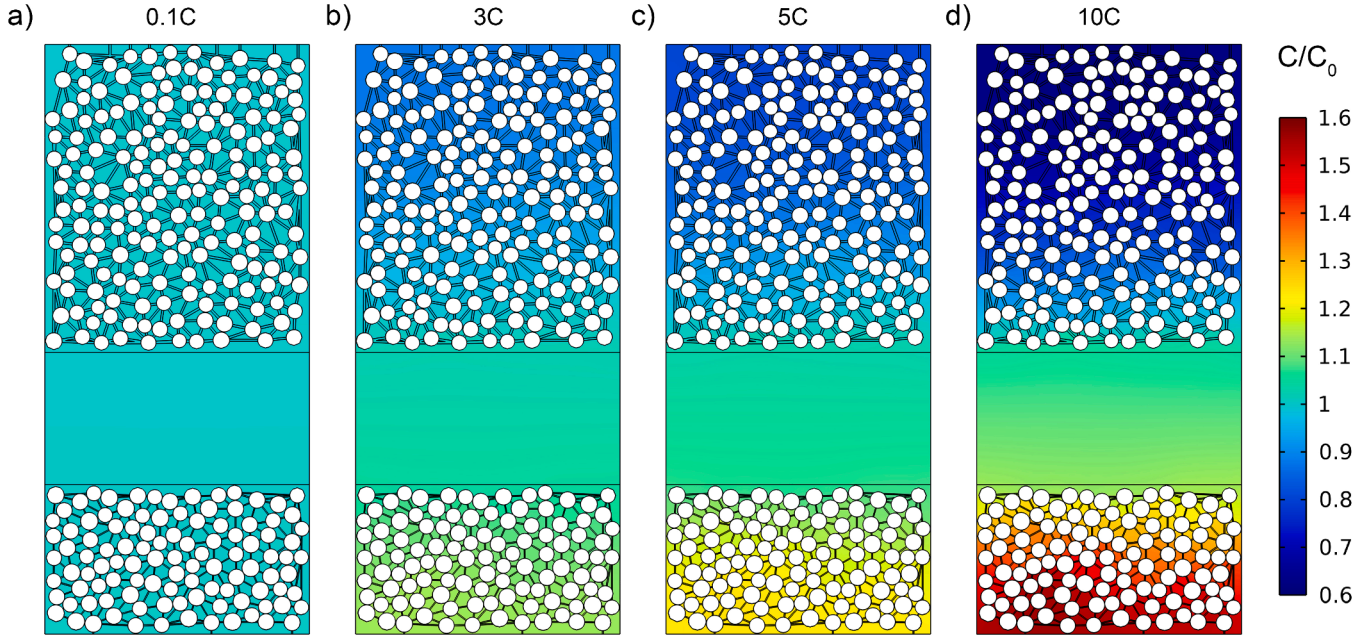

Fig. 9. The distribution of c_l of LFE||Gr batteries with $\sigma = 0.1$ at different C-rates and the end of discharging. a) 0.1C, b)3C, c) 5C, d) 10C.

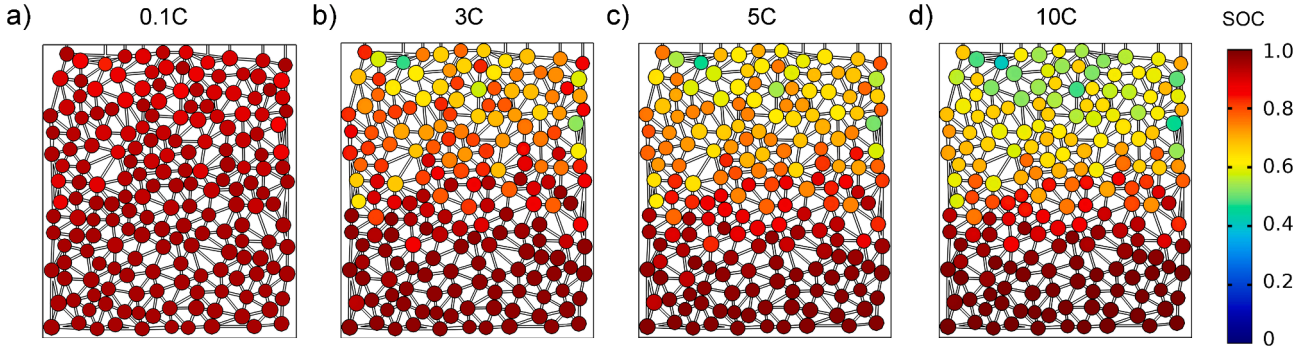

Fig. 10. The distribution of c_s of LFE electrodes with $\sigma = 0.1$ at different C-rates and the end of discharging. a) 0.1C, b)3C, c) 5C, d) 10C.

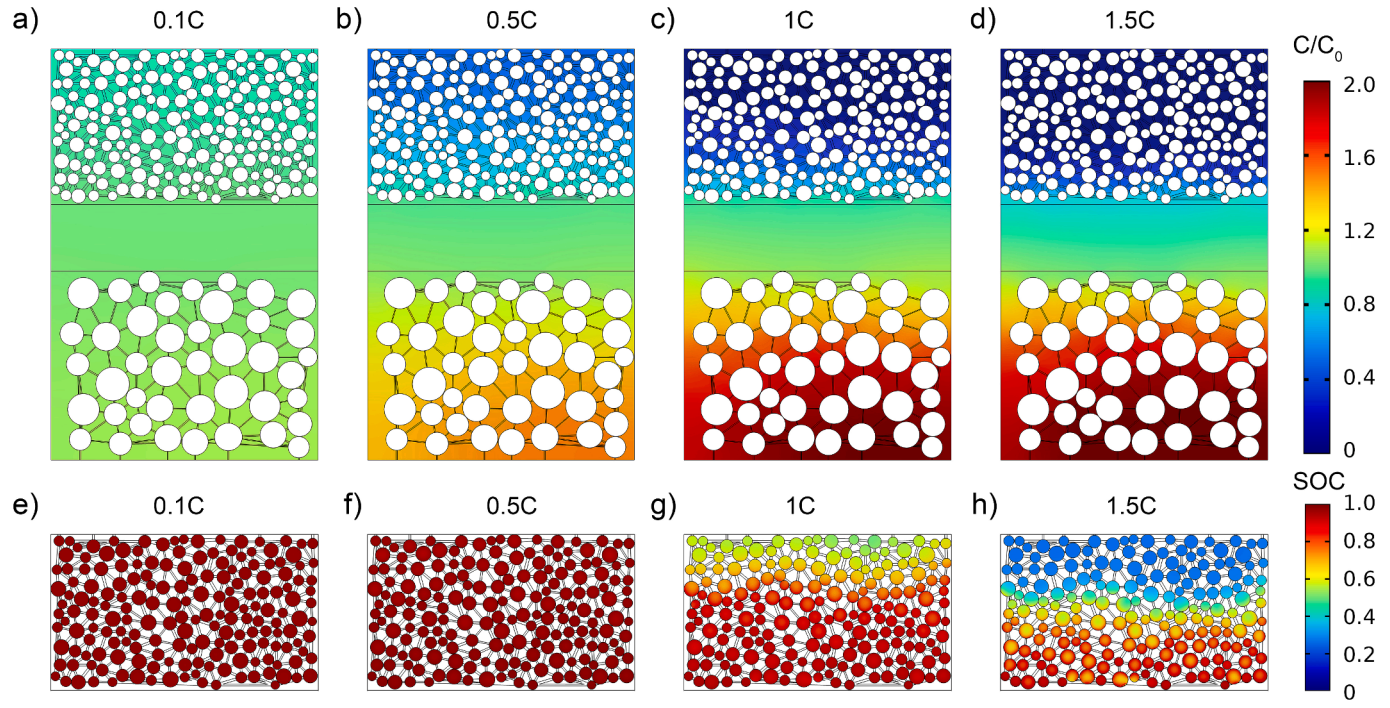

Fig. 11. The distribution of (a-d) c_l and (e-h) c_s of NCM||Gr batteries at different rates and the end of discharging. a) and e) 0.1C, b) and f) 0.5C, c) and g) 1C, d) and h) 1.5C.

significant difference when C-rate is lower than 2C. when the discharge current exceeds 5C, the capacity shows noticeable changes. Fig. 8b demonstrates that homogenizing the particle size can enhance the rate performance of LIBs. Fig. 9 shows the distribution of c_s of LFE electrode and Fig. 10 shows the distribution of c_l of LFE||Gr batteries with particle dispersion $\sigma = 0.1$ at different C-rates and the end of discharging. At 0.1C, the distributions of c_s and c_l with $\sigma = 0.1$ are homogeneous. However, at high C-rates of 10C, the concentration gradient of c_l is slightly higher than that with $\sigma = 0.3$. The polarization caused by this concentration gradient is smaller than that caused by the particle sizes. Therefore, enhancing particle uniformity can improve the C-rate performance of the LFE batteries in this work.

For the LFE system used in this work, the most significant factor affecting LIB performance is the inconsistency in particle sizes of the active materials. Thus, electrode structure optimization focuses on minimizing the heterogeneity among particle sizes. However, the NCM system considered in this work exhibits distinct characteristics.

Fig. 11 shows the distribution of c_l and c_s of NCM||Gr batteries at different C-rates and the end of discharging. Different with the LFE||Gr batteries, the impact of particle size on SOC of the NCM||Gr batteries is minimal, while C-rate plays a more significant role in the concentration gradient of c_l in the z-direction. At 0.1C, the concentration gradient of c_l is minimal and approaches negligible levels. When the C-rate is increased to 0.5C, a minor concentration gradient of c_l becomes apparent. Nonetheless, this gradient has an almost imperceptible impact on the concentration gradient of the c_s in the z-direction. In contrast, a notable concentration of active materials is observed in the r-direction, attributed to the lithium embedded from interfacial reactions that cannot diffuse rapidly within the active materials. This suggests that, at low C-rate (0.1C and 0.5C), the C-rate performance depends on the Li^+

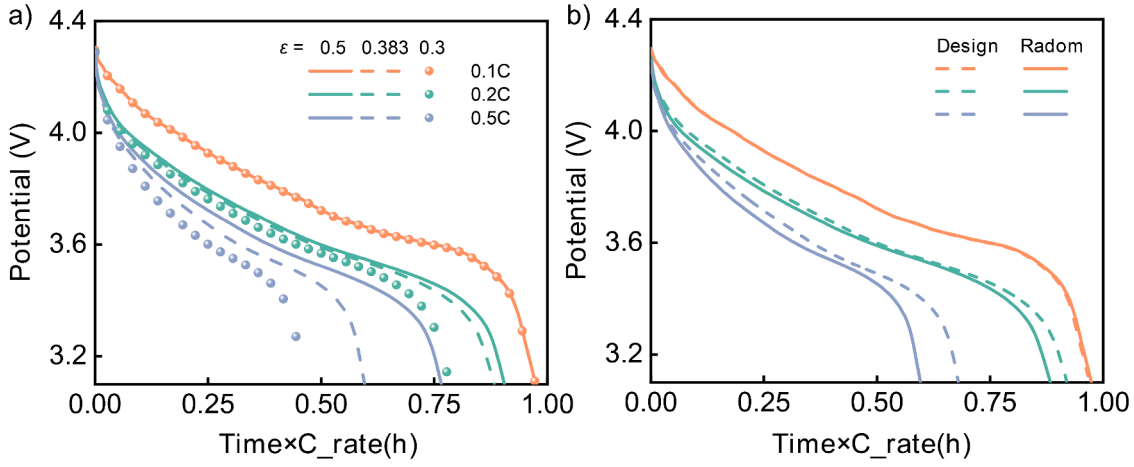

Fig. 12. a) The discharging curves of NCM||Gr batteries with different porosity ε and C-rates. b) The discharging curves of NCM||Gr batteries with different cathode structures. The solid lines and dashed lines correspond to the simulation results with the design ordered structure and randomized packing structure of the NCM electrode.

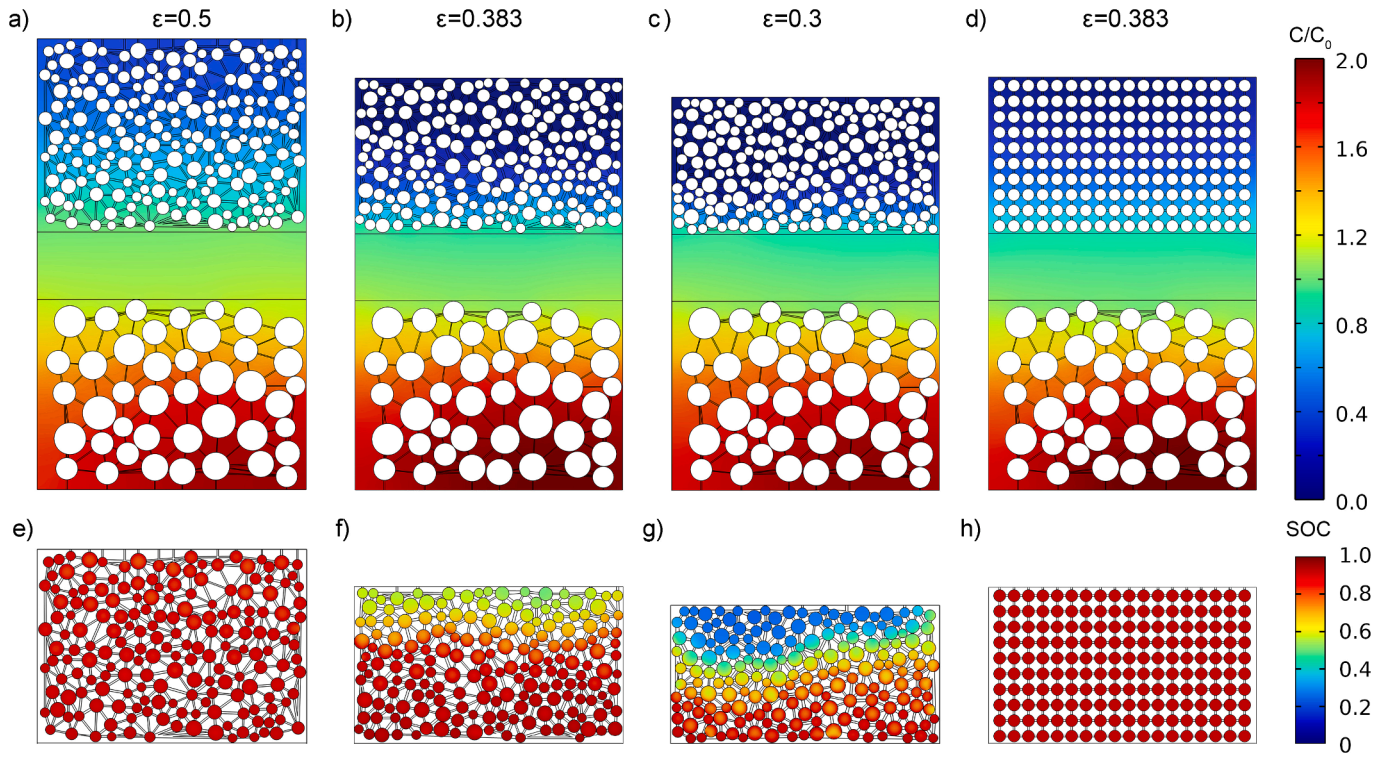

Fig. 13. The distribution of (a-c) c_l and (e-g) c_s of NCM||Gr batteries with different porosity at 1C and the end of discharging. a) and e) $\varepsilon = 0.5$, b) and f) $\varepsilon = 0.383$, c) and g) $\varepsilon = 0.3$. d) and h) The distribution of (a-c) c_l and (e-g) c_s of NCM||Gr batteries with the designed electrode at $\varepsilon = 0.383$, 1C and the end of discharging.

transfer in active material. At 1C and 1.5C, the c_l in some pores within the cathode approaches zero. The reduction reaction initially consumes Li^+ in the pores, while Li^+ de-intercalation from the anode fails to reach this area, resulting in incomplete charging of the active material. This observation implies that the C-rate performance depends on the Li^+ transfer in active material at high C-rates. Conversely, the Li^+ concentration and local potential near the separator increase, leading to the overcharging of active materials near the separator, abnormal Li deposition, and the growth of Li dendrites. Overcharging/overdischarging can cause the structural collapse of the active materials, resulting in irreversible capacity loss. The growth of lithium dendrites has the propensity to produce dead lithium and instigate short circuits, thereby intensifying gas generation and increasing the risk of leakage and explosion.

In this work, different porosities were also used to analyze the effect of porosity on the NCM batteries. Fig. 12a shows the discharging curves of NCM||Gr batteries with ε of 0.5, 0.383, and 0.3 at different C-rates, Fig. 13a-c show the corresponding distribution of c_l at 1C and Fig. 13e-g show the corresponding distribution of c_s at 1C. As the particle size of the NCM particles had minimal influence on the NCM system in this investigation, the C-rate performance declined as the porosity decreased. At 1C and $\varepsilon = 0.5$, the minimum value of c_l is greater than 0. At 1C and $\varepsilon = 0.383$, the c_l in some regions were zero. The ratio of the area with $c_l = 0$ to the area of the positive liquid phase increases with the increase of ε. Correspondingly, the proportion of incompletely charged active material particles increases and the capacity of the batteries decreases. The LFE||Gr batteries and NCM||Gr batteries utilized in this work have a commonality: localized concentration anomalies. This phenomenon primarily manifests as the incomplete charging of localized active material particles and the increase of c_l in specific regions, which is attributed to the non-uniform distribution of particles. Therefore, we designed a model for packing uniformly distributed particles, keeping its porosity, the volume of active materials and the volume of conductive binders consistent with the PPE model for $\varepsilon = 0.383$. This ordered structure both reduces the gradient variation of c_l in the z-direction and allows for uniform charging of the NCM particles (Fig. 13d and h).

4. Conclusion

In this work, we have constructed a physical-based particle packing electrode model. This model randomly packs active material particles based on actual particle sizes and constructs conductive networks based on volume fractions of conductive binders. With this strategy, the particle packing electrode model can accurately describe the microstructure of the electrode. Comparing the experimental and simulation data with different electrode materials and currents, the particle packing electrode model is more reliable than the pseudo-two-dimensions model. In the meantime, this two-dimensional porous electrode model can visually represent the local responses within the battery.

This work analyzes the charging dynamic of lithium-ion batteries at different C-rates. We found that, at low C-rates, the charge–discharge process is uniform and primarily controlled by reaction rates, whereas ion transport limits the charge–discharge of the active material particles at high C-rates. Within the batteries considered in this work, the particle size distribution of active material has a more significant effect on LFE|| graphite batteries, while the diffusion of Li^+ in the electrolyte has a more significant impact on NCM||graphite batteries. We propose that improving both the homogeneity of the particles and the ordering of the pore structure can enhance the performance of lithium-ion batteries. Notably, the optimization approaches are prioritized differently depending on the specific system. The particle packing electrode model provides theoretical insights for optimizing the microstructure of lithium-ion batteries to enhance their performance.

CRediT authorship contribution statement

Yiting Lin: Writing – original draft, Visualization, Methodology, Formal analysis, Data curation. **Yunqi Cai:** Writing – review & editing, Supervision, Software. **Cheng Lian:** Writing – review & editing,

Supervision, Resources, Investigation, Funding acquisition. **Honglai Liu:** Writing – review & editing, Supervision, Resources, Funding acquisition.

Declaration of competing interest

The authors declare that they have no known competing financial interests or personal relationships that could have appeared to influence the work reported in this paper.

Data availability

Data will be made available on request.

Acknowledgements

This work was sponsored by the National Key Research and Development Program of China (No. 2022YFA1503501), the National Natural Science Foundation of China (No. 22278127, 22378112), the Fundamental Research Funds for the Central Universities (No. 2022ZFJH004) and 21C Innovation Laboratory, Contemporary Amperex Technology Ltd by project No. 21C-368 OP-202312, Shanghai Pilot Proaram for Basic Research (22T01400100-18).

Appendix A. Supplementary data

Supplementary data to this article can be found online at https://doi.org/10.1016/j.ces.2024.120171.

References

Abdollahifar, M., Cavers, H., Scheffler, S., Diener, A., Lippke, M., Kwade, A., 2023. Adv. Energy Mater. 13, 2300973.
An, F., Zhou, W., Li, P., 2021. Electrochim. Acta 370.
G. Apachitei, M. Hidalgo, D. Dogaru, M. Lain, R. Heymer, J. Marco, M. Copley, Batteries, 10.3390/batteries9040192.
Bae, S., Song, H.D., Nam, I., Kim, G.-P., Lee, J.M., Yi, J., 2014. Chem. Eng. Sci. 118, 74.
Chang, Q., Fu, X., Gao, J., Zhang, Z., Liu, X., Huang, C., Li, Y., 2023. Adv. Mater. 35, 2305317.
Chen, Z., Danilov, D.L., Eichel, R.A., Notten, P.H.L., 2022. Adv. Energy Mater. 12.
Cheng, X., Tang, C., Yan, C., Du, J., Chen, A., Liu, X., Jewell, L., Zhang, Q., 2023. Mater. Today Nano 22.
Chung, D.-W., Shearing, P.R., Brandon, N.P., Harris, S.J., García, R.E., 2014. J. Electrochem. Soc. 161, A422.
Danner, T., Singh, M., Hein, S., Kaiser, J., Hahn, H., Latz, A., 2016. J. Power Sources 334, 191.
Duan, X., Li, B., Li, J., Gao, X., Wang, L., Xu, J., 2023. Adv. Energy Mater. 13.
Fang, R., Ge, H., Wang, Z., Li, Z., Zhang, J., 2020. J. Electrochem. Soc. 167.
Franco, A.A., 2013. RSC Adv. 3.
Fu, X., Zhou, Y., Huang, J., Feng, L., Yu, P., Zhang, Q., Yang, W., Wang, Y., 2023. Adv. Energy Mater. 13.
Grießl, D., Adam, A., Huber, K., Kwade, A., 2022. J. Electrochem. Soc. 169, 020531.
Hamed, H., Yari, S., D'Haen, J., Renner, F.U., Reddy, N., Hardy, A., Safari, M., 2020. Adv. Energy Mater. 10.
Huang, P., Tao, H., Yang, J., Lian, C., Liu, H., 2022. AIChE J. 68.
Kang, J., Gu, L., Wang, J.V., Wu, Z., Zhu, G., Li, Z., 2022. J. Power Sources 542.
Le Houx, J., Kramer, D., 2020. Energy Rep. 6, 1.
Le, T.D., Lasseux, D., Nguyen, X.P., Vignoles, G., Mano, N., Kuhn, A., 2017. Chem. Eng. Sci. 173, 153.
Li, W., Demir, I., Cao, D., Jöst, D., Ringbeck, F., Junker, M., Sauer, D.U., 2022. Energy Storage Mater. 44, 557.
Li, J., Wang, D., Pecht, M., 2019. J. Power Sources 436, 226885.
Lin, Y., Lian, C., Berrueta, M.U., Liu, H., van Roij, R., 2022. Phys. Rev. Lett. 128.
Lombardo, T., Ngandjong, A.C., Belhcen, A., Franco, A.A., 2021. Energy Storage Mater. 43, 337.
Lu, X., Zhang, X., Tan, C., Heenan, T.M.M., Lagnoni, M., O'Regan, K., Daemi, S., Bertei, A., Jones, H.G., Hinds, G., Park, J., Kendrick, E., Brett, D.J.L., Shearing, P.R., 2021. Energ. Environ. Sci. 14, 5929.
Lueth, S., Sauter, U.S., Bessler, W.G., 2015. J. Electrochem. Soc. 163, A210.
Mistry, A.N., Smith, K., Mukherjee, P.P., 2018. ACS Appl. Mater. Interfaces 10, 6317.
Narita, K., Citrin, M.A., Yang, H., Xia, X., Greer, J.R., 2020. Adv. Energy Mater. 11.
Newman, J., Tiedemann, W., 1975. AIChE J. 21, 25.
Nguyen, T.-T., Demortière, A., Fleutot, B., Delobel, B., Delacourt, C., Cooper, S.J., 2020. npj Comput. Mater. 6.
Pinilla, S., Ryan, S., McKeon, L., Lian, M., Vaesen, S., Roy, A., Schmitt, W., Coleman, J.N., Nicolosi, V., 2023. Adv. Energy Mater. 13, 2203747.
R. F. Service, 2019. Science 366, 292.
Safari, M., Delacourt, C., 2011. J. Electrochem. Soc. 158.
Shodiev, A., Chouchane, M., Gaberscek, M., Arcelus, O., Xu, J., Oularbi, H., Yu, J., Li, J., Morcrette, M., Franco, A.A., 2022. Energy Storage Mater. 47, 462.
Taiwo, O.O., Finegan, D.P., Gelb, J., Holzner, C., Brett, D.J.L., Shearing, P.R., 2016. Chem. Eng. Sci. 154, 27.
Tao, H., Lian, C., Liu, H., 2020. Green Energy Environ. 5, 303.
Trembacki, B.L., Mistry, A.N., Noble, D.R., Ferraro, M.E., Mukherjee, P.P., Roberts, S.A., 2018. J. Electrochem. Soc. 165, E725.
Wang, C.-Y., Liu, T., Yang, X.-G., Ge, S., Stanley, N.V., Rountree, E.S., Leng, Y., McCarthy, B.D., 2022. Nature 611, 485.
Weichert, A., Göken, V., Fromm, O., Beuse, T., Winter, M., Börner, M., 2022. J. Power Sources 551.
Winter, M., Barnett, B., Xu, K., 2018. Chem. Rev. 118, 11433.
Xia, R., Zhao, K., Kuo, L.-Y., Zhang, L., Cunha, D.M., Wang, Y., Huang, S., Zheng, J., Boukamp, B., Kaghazchi, P., Sun, C., ten Elshof, J.E., Huijben, M., 2022. Adv. Energy Mater. 12, 2102972.
Xu, J., Ngandjong, A.C., Liu, C., Zanotto, F.M., Arcelus, O., Demortière, A., Franco, A.A., 2023. J. Power Sources 554.
Yi, S., Yan, Z., Li, X., Wang, Z., Ning, P., Zhang, J., Huang, J., Yang, D., Du, N., 2023. Chem. Eng. J. 473, 145161.
Zhang, R., Wang, C., Zou, P., Lin, R., Ma, L., Li, T., Hwang, I.-H., Xu, W., Sun, C., Trask, S., Xin, H.L., 2023. Nat. Energy.
Zhang, Y., Zhao, W., Kang, C., Geng, S., Zhu, J., Xiao, X., Ma, Y., Huo, H., Zuo, P., Lou, S., Yin, G., 2023. Matter.